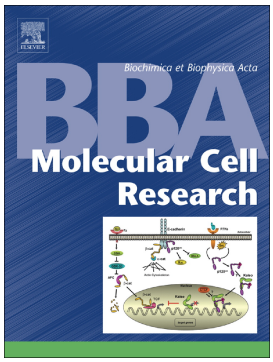

Fluorescence correlation spectroscopy reveals the dynamics of kinesins interacting with organelles during microtubule-dependent transport in cells

María Cecilia De Rossi, Nicolás González Bardeci, Yanina Álvarez, Esteban Mocksos, Juan José Romero, Luciana Bruno, Diana Elena Wetzler, Valeria Levi

PII: S0167-4889(19)30180-6

DOI: https://doi.org/10.1016/j.bbamcr.2019.118572

Reference: BBAMCR 118572

To appear in: *BBA - Molecular Cell Research*

Received date: 10 April 2019

Revised date: 4 September 2019

Accepted date: 20 September 2019

Please cite this article as: M.C. De Rossi, N.G. Bardeci, Y. Álvarez, et al., Fluorescence correlation spectroscopy reveals the dynamics of kinesins interacting with organelles during microtubule-dependent transport in cells, *BBA - Molecular Cell Research*(2019), https://doi.org/10.1016/j.bbamcr.2019.118572

Fluorescence correlation spectroscopy reveals the dynamics of kinesins interacting with organelles during microtubule-dependent transport in cells

María Cecilia De Rossi[a], Nicolás González Bardeci[a], Yanina Álvarez[a], Esteban Mocksos [c], Juan José Romero[a], Luciana Bruno[b], Diana Elena Wetzler[a], Valeria Levi[a*]

[a] Departamento de Química Biológica, Facultad de Ciencias Exactas y Naturales, Universidad de Buenos Aires. IQUIBICEN-CONICET. Ciudad de Buenos Aires, Argentina.

[b] Departamento de Física, Facultad de Ciencias Exactas y Naturales, Universidad de Buenos Aires. IFIBA-CONICET. Ciudad de Buenos Aires, Argentina.

[c] Departamento de Computación, Facultad de Ciencias Exactas y Naturales, Universidad de Buenos Aires. Centro de Simulación Computacional para Aplicaciones Tecnológicas (CSC) CONICET, Ciudad de Buenos Aires, Argentina.

[*]To whom correspondence should be addressed. E-mail: vlevi12@gmail.com. Phone and fax: 0054-114-786-3426.

Abstract

Microtubule-dependent motors usually work together to transport organelles through the crowded intracellular milieu. Thus, transport performance depends on how motors organize on the cargo. Unfortunately, the lack of methodologies capable of measuring this organization in cells determines that many aspects of the collective action of motors remain elusive. Here, we combined fluorescence fluctuations and single particle tracking techniques to address how kinesins organize on rod-like mitochondria moving along microtubules in cells. This methodology simultaneously provides mitochondria trajectories and EGFP-tagged kinesin-1 intensity at different mitochondrial positions with millisecond resolution. We show that kinesin exchange at the mitochondrion surface is within ~100 ms and depends on the organelle speed. During anterograde transport, the mitochondrial leading tip presents slower motor exchange in comparison to the rear tip. In contrast, retrograde mitochondria show similar exchange rates of kinesins at both tips. Numerical simulations provide theoretical support to these results and evidence that motors do not share the load equally during intracellular transport.

Keywords

Intracellular transport; molecular motors; kinesin-1; mitochondria; *Drosophila* S2 cells

Abbreviations

ACF, autocorrelation function, KHC, kinesin heavy chain; MTDR, mitotracker Deep Red FM; FCS, fluorescence correlation spectroscopy; EGFP, enhanced green fluorescent protein; EYFP, enhanced yellow fluorescent protein.

1. Introduction

Intracellular transport relies on molecular motors that actively step along cytoskeletal filaments dragging cargoes through the crowded cytoplasm (reviewed in [1-3]). Particularly, kinesins and dyneins move along microtubules toward the plus and minus ends of these filaments, respectively (reviewed in [4]). Transport impairment in many neurodegenerative diseases such as

Alzheimer's, Huntington's and Parkinson's highlights the relevance of understanding how motors work in the cellular context [5-7].

The properties of microtubule-dependent motors have been extensively studied with single-molecule techniques that provided exquisite biomechanical information such as the stall force, step size and processivity; many of these determinations were done incorporating the motors in synthetic systems designed to mimic some of the features of the intracellular transport [8-17].

Advances in fluorescence microscopy methods allowed the observation of single motor molecules in living cells. Different labeling strategies, including the use of relatively big fluorescent quantum dots [18] or tandems of fluorescent proteins [19, 20], were necessary to improve the signal to noise (S/N) ratio and reach the single molecule regime. Although the engineering of the motors resulted in their inability to bind natural cargoes, those works provided essential information on single motor performance in their natural environment and opened new questions on how motors work when dragging a cargo in the crowded intracellular milieu.

Recent studies suggest that the spatial distribution of motors and their mechanical communication through the surface of the cargo may have an impact on transport. For example, Rai et al. [21] found that dynein motors cluster on raft-like domains of phagosome membranes and, as a consequence, improve their performance as a team. *In vitro* assays also indicated that the efficiency of collective transport is modulated by the fluidity of the membrane that controls the motors mobility [22, 23]. More recently, Kaplan et al. [24] pointed out that rotational motion of endosomes tagged with gold nanorods induced by motor activities correlate with the translational dynamics of the cargo. Taken together, these studies emphasize the relevance of the organization of motors on the cargo and stress the necessity of characterizing their dynamical distribution in living cells.

In this work, we use a combination of single particle tracking and fluorescence fluctuations methods to assess the dynamics of kinesin molecules on organelles while they move along microtubules in *Drosophila melanogaster* S2 cells. These cells, generated from late stage embryos of OregonR *Drosophila melanogaster* [25], present several advantages that make them ideal for the analysis of cellular processes [25, 26]. Briefly, culturing the cells and observing them in optical microscopy experiments is extremely simple since they grow at 25 °C and do not require injection of CO_2 in the atmosphere allowing their observation for long periods of time at room conditions. They are highly transfectable making it easy to generate stable cell lines and to express proteins of interest tagged with fluorescent probes to be used in fluorescence microscopy experiments. Additionally, these cells are also very sensitive to RNAi treatments allowing an efficient knockdown of proteins of interest. Since these cells normally grow loosely attached, S2 cells are usually spread onto coverslips coated with concanavalin A that promotes the attachment of the cells for microscopy observations. In this condition, S2 cells flatten and the thinner periphery becomes ideal for live-cell observations. After disruption of their actin network with

drugs such as cytochalasin D or latrunculin B, S2 cells produce long processes filled with uniformly polarized microtubules [27, 28] making them an excellent system to study microtubule-dependent transport [27-34].

Importantly, Rogers et al. [35] showed that the morphology of the interphase microtubule network in S2 and other *Drosophila* cells is different from that observed in many mammalian cells (i.e. microtubules emanating from a centrosome located near the nucleus in a star-like structure with their plus ends pointing outward and growing toward the cell periphery [36]). Indeed, functional centrosomes in *Drosophila* cells are only present during mitosis whereas microtubules nucleate at specific sites in the cytoplasm during interphase [35]. Centrosomes were initially considered essential for the assembly of mitotic spindle in most animal somatic cells. The textbook mechanism indicated that these structures duplicate before the entry to mitosis, separate and recruit additional pericentriolar material that initiate more centrosome-associated microtubules leading to spindle assembly [37, 38]. However, it is now well established that centrosomes are not essential for the assembly of the mitotic spindle (see for example, [39-41]).

The versatility of Drosophila S2 cells allowed studying mitosis through a combination of techniques including genome-wide screening, RNA interference assays, fluorescence microscopy and, more recently, transmission electron microscopy [35, 42-61]. Particularly, Moutinho-Pereira et al [47] showed that a same set of genes is involved in centrosome-dependent and independent pathway of spindle assembly in this cell line, with only a small number of genes required exclusively for acentrosomal assembly. In the case of S2 cells, the centrosome-based nucleation is the dominant pathway but it is proposed to coexist with mechanisms involving chromosome-based assembly and recruitment of microtubules created at other sites [42]. The existence of redundant pathways for creating the spindle would improve the chances of a successful mitosis [37, 42].

We should emphasize that mitosis in S2 cells shows distinct characteristics with respect to other lines. Indeed, half of the cells present more than two centrosomes at the onset of mitosis and a clustering/fusion process occurs during spindle assembly [44]. This clustering process is occasionally incomplete consequently generating multipolar spindles during prometaphase. This fact increases the probability of misaligned chromosomes in metaphase [44, 51] resulting also in a relatively proportion of cells with atypical spindles [44, 45]. Several distinctive characteristics of S2 cells, including a cell cycle with other differences from those of mammalian cells (e.g. [43, 56, 62, 63]), indicate that caution is required when extrapolating or generalizing experimental observations in this cell system to other cell lines.

We focused our studies on mitochondria, organelles involved in the generation of ATP with key roles in lipid metabolism, calcium homeostasis and cell differentiation among many other processes [64, 65]. Molecular motors contribute to the regulation of their size and shape [66, 67]

which are essential aspects for the cell homeostasis [68]. It has been proposed that mitochondria bind kinesin-1, kinesin-3 and cytoplasmic dynein in neurons [69-71]; the interaction requires adaptor proteins such as the Miro-Milton complex and KBP that modulate the number of motors attached to the cargo and/or their activity [72].

Our data reveal that the exchange of kinesin motors on single organelles during active transport in living cells is in the order of ~ 100 ms. Additionally, we verified that the dwell time at the leading and rear ends of mitochondria moving along microtubule bundles in cell processes depends on the transport direction. Particularly, anterograde organelles present slower exchange rates at the leading tip whereas retrograde mitochondria show similar rates at the leading and rear tips. These results agree with the predictions of a numerical model of kinesins collectively working against load and support that motors dragging a cargo do not share the load equally in living cells. Together our data provide valuable information on how molecular motors organize on cargoes moving along microtubules in the crowded cell cytoplasm.

2. Materials and methods

2.1 Molecular cloning

Full-length *Drosophila* KHC (amino acids 1–975) contained in a pMT-KHC-RFP plasmid was subcloned KpnI-EcoRI into the $CuSO_4$ inducible pMT-C (Invitrogen) to generate pMT-KHC. EGFP sequence from pEGFP-N3 (Clonech) was subcloned into the pMT-KHC using the EcoRI and NotI restriction sites obtaining the pMT-KHC-EGFP vector. The pMT-KHC-RFP plasmid was a kind gift from Dr. Vladimir I Gelfand (Northwestern University, Chicago, IL).

2.2 Cells culture and transfections

Drosophila S2 cells were cultured as previously described [29]. Cells were grown in Schneider's Media (Sigma-Aldrich) supplemented with 10% FBS. Transient transfections of KHC-EGFP or EYFP-mito [73] were performed using Effectene (QIAGEN) following the vendor instructions. KHC-EGFP expression was induced adding to the medium 0.4 mM $CuSO_4$ (final concentration) 24 h before imaging.

EYFP-mito plasmid encodes the mitochondrial targeting sequence from subunit VIII of human cytochrome c oxidase fused to EYFP [74] and was a kind gift from Dr. Kristin White (MGH/Harvard Medical School, Charlestown, MA).

2.3 Cells preparation for imaging experiments

For microscopy measurements, 25-mm round coverslips previously modified with 500 μg/ml of concanavalin A (Sigma-Aldrich) were mounted in a custom-made chamber specially designed for the microscope. Cells were added to the chamber and incubated in 0.5 ml of serum-free medium containing 10 mM of latrunculin B (Sigma-Aldrich) for 15 min to depolymerize actin filaments. After the cells adhered to the coverslips, 100 nM of MitoTracker Deep Red FM (Invitrogen) was added to the incubation medium for mitochondria labeling. To depolymerize microtubules, cells were incubated 30 min at 0 °C with 10 μM nocodazole [75]. Intracellular ATP concentration was reduced by incubating cells during 60 min at 37 °C with 20 mM azide [76].

2.4 Isolation of mitochondria

A suspension enriched in mitochondria was obtained following the procedure described in [77, 78] with some modifications. *Drosophila* S2 cells grown in T-25 culture flask to ~80-90 % confluency were collected by centrifugation at 500 g, washed with PBS, and suspended in 1 mL of cold (4 ^{o}C) lysis buffer (Hepes 10 mM pH 7.4, 250 mM sucrose, 1 mM EDTA, 1 mM EGTA, and a protease inhibitor cocktail containing 10 μg/mL aprotinin, 10 μg/mL leupeptin, 1 mM PMSF). The cell suspension was passed through a 26-gauge needle to lyse the cells and centrifuged during 10 min at 1000 g to remove cellular debris. The supernatant was centrifuged 20 min at 12000 g to obtain a pellet enriched in mitochondria that was washed and suspended in lysis buffer.

2.5 Confocal microscopy

Confocal images were acquired in a FV1000 Olympus confocal microscope (Olympus Inc., Japan). EGFP or EYFP fusion proteins and MitoTracker Deep Red FM were observed using a multi-line Ar laser tuned at 488 nm and a diode laser of 635 nm (average power at the sample, 2 μW and 0.2 μW, respectively) as excitation source, respectively. The laser light was reflected by a dichroic mirror (DM 405/488/543/635) and focused through an Olympus UPlanSApo 60× oil immersion objective (NA = 1.35) onto the sample. Fluorescence was collected by the same objective and split into two channels set to collect photons in the range 500–525 nm (green channel, EGFP or EYFP) and 650–750 nm (red channel, MTDR).

The alignment of the channels was evaluated measuring the intensity profiles of small mitochondria (i.e. those with image sizes close to that expected for the Airy disk) in cells expressing EYFP-mito and labeled with MTDR (Supplemental Fig. 1). This approximation is valid since both fluorescent molecules localize in inner regions of mitochondria. We observed a slight shift between channels of ~80 nm that is not expected to affect significantly the FCS

analyses of KHC-EGFP since the ACF curves are calculated after binning the intensity of 5 contiguous pixels in the line as will be described below.

2.6 Fluorescence Correlation Spectroscopy

FCS measurements were performed in an Olympus FV1000 confocal microscope set in the pseudo photon-counting mode. The lasers power was set to 9.7 μW (488 nm) and 3.5 μW (635 nm), respectively.

The autocorrelation function was calculated as:

$$G(\tau) = \frac{\langle \delta I(t) \cdot \delta I(t+\tau) \rangle}{\langle I(t) \rangle^2} \qquad (1)$$

where I(t) represents the fluorescence intensity at time t, the brackets indicate average values over the time-course of the experiment, and $\delta I(t)=I(t)-\langle I(t) \rangle$ represents the fluorescence intensity fluctuation at time t.

The point-FCS data was collected at a frequency of 10^5 Hz during ~3 min. These data was fitted with a model that considers two populations of molecules diffusing in different time scales [79]:

$$G(\tau) = \frac{\gamma}{N}\left[f_{fast}\left(1+\frac{\tau}{\tau_{D,fast}}\right)^{-1}\left(1+\frac{\tau}{\omega^2\tau_{D,fast}}\right)^{-1/2} + f_{slow}\left(1+\frac{\tau}{\tau_{D,slow}}\right)^{-1}\left(1+\frac{\tau}{\omega^2\tau_{D,slow}}\right)^{-1/2}\right] \qquad (2)$$

where N is the average number of KHC-EGFP molecules within the detection volume, γ is a geometric factor set to 0.35 for a confocal setup, ω is the ratio between the axial (ω_z) and equatorial ($\omega_{x,y}$) radii of the observation volume and $\tau_{D,fast(slow)}$ is the characteristic diffusion time of fast (slow) molecules. This last parameter is related to the diffusion coefficient (D) of the molecules as follows:

$$\tau_{D,fast(slow)} = \frac{\omega_{xy}^2}{4D_{fast(slow)}} \qquad (3)$$

where $D_{fast(slow)}$ is the diffusion coefficient of the fast(slow) molecules.

The mean cytoplasmic concentration of fluorescent KHC-EGFP was estimated using the value of N determined from the fit of the point-FCS correlation curves with Eq. 3 and considering the confocal observation volume as $V= \pi^{3/2}\omega_{x,y}{}^2\omega_z/\sqrt{8}$ [80] which was calibrated as previously described [81].

In line-scanning FCS experiments, the lasers simultaneously and repetitively scanned 10^4 lines along the process (pixel size = 41 nm, line length range = 5-10 μm). The line acquisition

frequency was in the range of 250-500 Hz. EGFP and MTDR fluorescence were collected as indicated above and these data were used to generate green and red kymographs, respectively. We analyzed rod-like mitochondria with image lengths longer than 900 nm unless explicitly indicated.

2.7 Kymograph analyses

We selected regions in the red-kymograph showing persistent, unidirectional motion of mitochondria for > 1.5 s, recovered the mitochondrion position in each line of the kymograph segment [82] with ~ 10 nanometer accuracy as assessed in control experiments with fixed cells and used this data to generate new green and red kymographs centered at the organelle central position. Intensity fluctuations of KHC-EGFP at different mitochondrion positions were computed selecting simultaneously the positions in the centered red and green kymographs. These fluctuations were analyzed through an autocorrelation analysis as described below.

FCS analyses at the mitochondria extremes were performed selecting regions of 5 pixels (205 nm) in the centered kymographs that included either the rear or the leading tip of the organelles. The green-channel intensity at these regions was calculated as a function of time adding up the counts registered in the pixels included in these regions line-by-line.

The autocorrelation function was calculated using the SimFCS program (LFD, Irvine, CA, USA) and fitted with the following equation:

$$G(\tau) = A\left[e^{-\tau/\tau_r} \right] + G_\infty \qquad (4)$$

where τ_r is the characteristic residence time of the fluorescent molecules in the confocal volume, A is a constant related to the mean number of fluctuating fluorescent molecules and G_∞ is the residual autocorrelation [83], this last parameter may be slightly different from zero due to limited statistics.

This expression is derived from [84] and considers randomly diffusing fluorescent molecules that slowly bind to immobile targets. In addition, the model assumes that the characteristic diffusion time is smaller than the sampling time as described in the text.

2.8 Trajectories analyses

We selected sections of mitochondria trajectories presenting both, processive motion and defined beginning and end positions. These runs were classified according to the direction of movement into anterograde (toward the tip of a process) and retrograde (toward the cell body) motion. The organelles speed, run length and run time were computed from a linear fit of the distance vs. time plot.

2.9 Numerical simulations

Numerical simulations of organelles transport along microtubules were based on stochastic models previously described in the literature [28, 85-87] with the parameter values compiled in Supplemental Table 1.

Briefly, we assumed a cargo driven along a 1D track by a team of 10 kinesin motors acting as parallel springs with elastic constant κ_0. The motors move stochastically in discrete 8-nm steps along the track, with probabilities of stepping and detachment depending on the load [85, 88, 89]. Motors do not diffuse when anchored to the microtubule to resemble their interaction to membrane domains with constrained motion [21, 24]. Unbound motors can rebind to the track with a constant probability or diffuse along the cargo membrane with a diffusion constant of 0.5 $\mu m^2/s$; this value is in the order of those determined for proteins anchored or attached to biological membranes (e.g. [22, 90]).

We considered periodic boundary conditions for the diffusing motors, i.e. motors reaching the tip of the cargo are replaced by new motor molecules at the opposite tip.

The simulations also assumed that the cargo moves in a viscous environment introducing a velocity-dependent drag on the cargo. Particularly, the viscosity value was set at $500x\eta_{H2O}$ with η_{H2O} corresponding to the viscosity of water, since the gel-like structure of the cytoplasm hinders the motion of particles [91] and therefore the apparent cytoplasmic viscosity depends on the particle size. Previous studies in different cell lines reported $\eta_{citoplasm}$ values ranging from $30x\eta_{H2O}$ (probe size 25nm, [91]) to $2500x\eta_{H2O}$ (probe size 1 μm, [92]).

Since opposed-polarity motors may also pull the organelle, we modeled the force introduced by the opposed team (i.e. dyneins) as: a) an additional, constant load or b) incorporating to the model 10 opposed-polarity motors that undergo a tug of war with the kinesin team.

After each simulation step (time step = 50 μs), we computed the kinesin motors' positions along the microtubule and generated a matrix containing the position of the motors along the simulated organelle as a function of time. These data sets were used as the input for the FERNET software [93] set in the line scanning mode (line time= 4 ms, pixel size= 42 nm) to obtain simulated intensity kymographs that were analyzed similarly to the experimental data.

2.10 Statistical analysis

To compare the median values (med) of different data sets, we used a hypothesis test computing the p-values as follows [87]:

$$p\text{-value} = 2\left[1 - \mathrm{F}\left(\frac{|\mathrm{med}_{(g1)} - \mathrm{med}_{(g2)}|}{\sqrt{\sigma^2_{(g1)} + \sigma^2_{(g2)}}}\right)\right] \quad (5)$$

where F is the standard normal distribution and σ^2 (g1) and σ^2 (g2) represent the variance of each data group.

The parameters' errors and variance were computed by a bootstrap procedure [94]. When residuals did not follow normal distribution and homogeneity of variance, transformation of data [95] was applied to meet both assumptions. Statistical data analysis was performed using the R software.

3. Results

3.1 Line-FCS experiments allow capturing the dynamics of motor molecules on actively transported organelles

In order to explore the dynamics of kinesin motors during mitochondria transport, we transfected *Drosophila* S2 cells with a plasmid encoding the full-length kinesin heavy chain (KHC) fused to EGFP. These cells were treated with latrunculin to generate cell processes containing microtubule bundles, labeled with Mitotracker Deep Red FM (MTDR) to stain mitochondria and imaged through confocal microscopy.

Fig. 1A shows that KHC-EGFP partitions between free and microtubule-associated pools as observed with other kinesin constructs [20]. It has been demonstrated that free KHC molecules are in an inactive, folded conformation [96-102]. This inactivation is achieved through an autoinhibitory mechanism that involves the interaction between the QIAKPIRP sequence of the tail domain and the Switch I region in the head of the KHC chain [100] and is released by interaction with the cargo (reviewed in [103]). The inactive motor has a low probability of binding to microtubules and thus the autoinhibitory mechanism avoids futile ATP consumption and guarantees a correct distribution of kinesin molecules within the cell [96, 103]. Therefore, the free KHC-EGFP pool probably consists of inactive molecules whereas the microtubule-associated pool corresponds to KHC-EGFP molecules also attached to a variety of intracellular cargoes.

Microtubules in S2 cells extend toward the cell periphery with their plus ends oriented to the cell periphery [35, 104]; microtubule bundles in the cell processes generated after depolymerization of actin also present a similar polarization as described before.

Time-lapse imaging indicates that mitochondria actively move along cellular processes in the transfected cells (Fig. 1B). We tracked mitochondria as described in Materials and Methods to

analyze if KHC-EGFP affects their transport and found that the expression of the motor did not modify their median speed, run time and run length (Supplemental Table 2).

Fig. 1C includes two snapshots of a representative time-lapse movie and plots of the intensity collected in the green (KHC-EGFP) and red (MTDR) channels along the process. The intensity profiles show a higher concentration of KHC-EGFP at mitochondrial positions suggesting that the fluorescent motors attach to these organelles. To confirm this result, we labeled the transfected cells with MTDR and prepared a suspension enriched in mitochondria as described in Materials and Methods. Confocal images of this sample showed a clear colocalization of KHC-EGFP molecules with mitochondria (Fig. 1D). This result agrees with previous observations showing that isolated mitochondria preserve kinesin motors on their membrane [70, 105, 106] and suggests that EGFP-labeled motors have a high affinity for these organelles. We should also mention that other organelles also show strong motor-organelle interactions. For example, a variety of purified organelles including melanosomes [107] phagosomes [108, 109] and lipid droplets [110] move directionally along microtubules adsorbed onto a coverslip indicating that motors remain anchored to organelles and preserve their activity. Optical trapping experiments of organelles in living cells also support this statement [110-112].

Next, we designed a fluorescence correlation spectroscopy (FCS) based approach to explore the dynamical organization of KHC-EGFP on mitochondria during their active motion along microtubule bundles in cell processes.

For the studies described below, we selected those cells expressing relatively low levels of fusion proteins since the amplitude of the correlation function depends inversely on the local concentration of fluorescent molecules [113]. Additionally, the mean cytoplasmic concentration of KHC-EGFP was estimated by point-FCS experiments (see Materials and Methods) obtaining a value of 820 ± 80 nM (N_{cells}= 7) which is in the order of the concentration estimated for endogenous kinesin in other cellular systems [114]. Importantly, the preservation of the overall cellular morphology and of relevant mitochondrial transport parameters (Supplemental Table 2) indicates that these levels of fluorescent kinesins do not produce aberrant transport behaviors.

The confocal microscope was set to run repetitive line-scans along single cell processes and to register simultaneously the fluorescence of KHC-EGFP and MTDR in independent detectors. This methodology allows collecting the fluorescence intensities at every position of the process with millisecond resolution in contrast to the second-scale resolution achievable by standard imaging. Fig. 2A shows a representative example of an intensity kymograph recovered from the red channel showing a mitochondrion that presents periods of active transport, reversions and pauses.

We focused our analyses in regions of the kymograph showing unidirectional motion and assigned the organelle direction according to the relative positions of the cell body and tip of the process. Then, the position of the organelle center was recovered with nanometer precision as

described in Materials and Methods and used to re-center the kymograph at the position determined for the organelle centroid; Supplemental Fig. 2 schematizes this procedure. The same transformation was applied to the kymograph obtained in the green channel. This transformation allowed recovering the intensity of KHC-EGFP at different mitochondrion positions as a function of time while the organelle moves directionally along the track.

The relatively high signal/noise ratio of the green-kymograph allows detecting a dimmer region in its central part. This result is similar to that obtained for an outer-membrane mitochondrial protein in a different cell system [115] and could be explained considering that fluorescent KHC molecules distribute on the surface of these organelles but not in their interior. Since the laser moves along the mitochondrial major axis, the beam center only intersects the outer membrane at the organelle tips showing relatively higher fluorescence intensities at these positions in comparison to the observed at regions in which the laser is mainly centered at the mitochondrial matrix. To test this proposition, we used the combination of CellBlender 1.1, MCell 3.2.1 [116-118] and FERNET 1.4 [93] to run simulations of line-scanning experiments in which the observation volume moved along an elongated organelle with a minor axis similar to those reported for mitochondria (in the range of 0.5-1 μm, [119]) and decorated with fluorescent molecules that diffused on its surface. Supplemental Fig. 3 shows that these simulations also predict a dimmer central region in the kymographs agreeing with the experimental observations.

Fig. 2B exemplifies the intensity trace and the autocorrelation function measured at a position close to the leading end of a mitochondrion; the correlation decays with the lag time indicating that KHC-EGFP dynamically exchanges during the active transport of the mitochondrion. We should mention that the number of data points included in the autocorrelation analysis is limited by the duration of anterograde and retrograde runs (~3 s, Supplemental Table 2); this natural constraint increases the noise of autocorrelation function and limits the temporal window of our observations.

As a control, we ran similar experiments in *Drosophila* S2 cells expressing EYFP-mito, an EYFP construct specifically targeted to the inner membrane of mitochondria. Single molecule tracking experiments showed that these mitochondrial proteins are almost immobile or present very small diffusion coefficients (data compiled in [120]). Supplemental Fig. 4 shows that the intensity collected for EYFP-mito diminished as a function of time. As EYFP-mito molecules are continuously illuminated, they photobleach and cannot be replaced by bright molecules within the time window of our experiments introducing the decay in the intensity trace, in agreement with the extremely slow and constrained motion expected for this protein [120, 121]. Consequently, the autocorrelation function does not relax and detrending routines are required to remove the photobleaching from the intensity traces (Supplemental Fig. 5). These results show that molecules anchored to mitochondria and with slow diffusion do not produce autocorrelation curves as those observed with fluorescent KHC which is then involved in different dynamical processes.

Fig. 2C schematizes the processes that might introduce KHC-EGFP intensity fluctuations in our experimental system. Particularly, motors may diffuse on the organelle membrane (i), bind and unbind from this membrane (ii), diffuse in the intracellular milieu (iii) or transport a cargo (iv). As mentioned before, free KHC molecules are in an autoinhibited conformation and do not interact with microtubules. Different experimental evidences allowed ruling out some of these processes as source of intensity fluctuations in our experimental conditions.

First, Fig. 1D shows that KHC-EGFP has high affinity for mitochondria supporting the absence of exchange of motors between organelles and the cytoplasmic pool (ii in Fig. 2C) within the temporal window of the FCS experiments. Second, most of the autocorrelation curves collected on mitochondria with optical sizes in the range 500-800 nm, i.e. similar to the dimensions of the confocal volume, did not decay to zero (65 %, N = 37) suggesting that KHC-EGFP molecules remain within the observation volume in the studied temporal window.

On the other hand, the expected size of the fluorescently labeled motor [122] and the intracellular viscosity [123] suggest that the millisecond time resolution of line-FCS experiments does not allow observing the diffusion of free KHC-EGFP molecules (iii in Fig. 2C). To evaluate this statement, we ran point-FCS experiments in cells expressing KHC-EGFP. These data could be fitted with a simple two-component diffusion model [79] suggesting the presence of at least two populations of molecules with different mobility (Fig. 2D); the slowest motion probably arises from KHC-EGFP molecules attached to intracellular targets whereas the fast component (characteristic time ~ 2 ms, Eq. 2 and 3) is compatible with the time scale expected for the diffusion of the labeled molecules. Supporting this statement, Supplemental Fig. 6 shows that microtubule depolymerization modified the dynamics of the slow component but did not affect the fast component as would be expected if this term were caused by the diffusion of free KHC-EGFP molecules. We should also mention that microtubule depolymerization is not expected to affect significantly the viscosity of the cytoplasm [124] and thus the diffusion of relatively small molecules. Indeed, the comparison of Fig. 2C and 2D indicates that this fast component could not be observed with the lower temporal resolution of line-FCS experiments. Also, ACF analyses presented no correlation at line positions that did not show mitochondria or other organelles detectable in the transmission image collected simultaneously in the confocal microscope (Supplemental Fig. 7A). We cannot discard the presence of other organelles that could interact with KHC-EGFP; these organelles are not labeled with fluorescent probes and may not be observed in our experimental conditions. We also performed line-FCS experiments in ATP-depleted cells; organelle transport stops in this condition since molecular motors require ATP to step along the track. Supplemental Fig. 7B showed that no correlation is observed at positions in which organelles were not detected also supporting that the diffusion of unbound motors is faster than the time resolution of our experiments.

To analyze if KHC-EGFP intensity fluctuations are related to mitochondrial transport, we compared the dynamics of KHC-EGFP on stationary and relatively slow organelles (speed < 50 nm/s) with that observed in fast, anterograde organelles (speed > 50 nm/s).

We fitted the experimental autocorrelation curves with Eq. 4 and recovered the characteristic residence time of KHC-EGFP molecules (τ_r) from this fitting (see Materials and Methods). Fig. 2E shows that τ_r was significantly smaller for fast-moving organelles suggesting that kinesin motors exchange faster when mitochondria actively move along microtubules. This result could be explained considering that motors attached to slow moving organelles are in a tie tug-of-war condition and thus they remain anchored to a position of the microtubule for longer periods of time [86, 125].

Therefore, we conclude that τ_r could sense changes in the dynamics of motors stepping along the microtubule carrying the cargo (iv in Fig. 2C) that may also detach from the track and diffuse on the organelle membrane (i in Fig. 2C).

FCS provides dynamical information with diffraction-limited spatial resolution (~200 nm lateral and ~1 μm axial, [126]). When the system is simple enough, it is possible to fit the experimental data with an equation derived from a theoretical model accounting for the mechanism involved in the fluctuations and obtained quantitative information of this mechanism. Unfortunately, this approximation is not valid for complex processes as that studied in our work. On the other hand, the dimensions of cell processes and mitochondria are similar to the confocal observation volume and thus the autocorrelation data critically depends on certain geometrical parameters such as the width of the cell processes [127] and the size and shape of mitochondria. Therefore, Eq. 4 only provides an estimation of the residence time of KHC-EGFP in the sampled region of the organelle but does not inform on quantitative parameters such as binding/unbinding rates to the microtubule. In spite of these limitations, the results showed in this section indicate that the correlation analyses allow sensing the motor dynamics at actively moving organelles and its relation to the transport.

3.2 KHC dynamics at the tips of motor-driven mitochondria depends on the transport direction

We next asked if KHC-EGFP dynamics on mitochondria actively moving along microtubules is similar at different organelle regions. This behavior would be expected when motors share the load equally [128] whereas a different dynamics at the organelle tips is predicted otherwise.

We tracked relatively long (1-2.5 μm) anterograde and retrograde mitochondria as described previously; Fig. 3A shows a representative autocorrelation matrix obtained by performing a pixel-by-pixel autocorrelation analysis in a region including a mitochondrion. This datum

suggests variations on the autocorrelation function and thus on the dynamics of KHC-EGFP at different regions of the organelle.

To improve the S/N ratio in the autocorrelation calculation at the organelle extremes, we selected regions of 5 pixels of the centered kymographs each one of them including the leading or rear end of the organelle. The observation volumes included in these regions did not overlap as inferred from the organelle lengths and the size of the confocal volume. We added up the intensity registered at the pixels included in each of these regions and obtained intensity traces at the leading and rear end of the mitochondria as a function of time. These traces were examined through an autocorrelation analysis (Fig. 3B).

Fig. 3C shows that the dynamics of KHC-EGFP at the leading edge of mitochondria was significantly slower than that observed at the rear end during anterograde transport. In contrast, the exchange of motors at the leading and rear ends were similar when the organelles moved in the opposite direction.

We also calculated the ratio between τ_r values measured in the same mitochondrion at the leading and rear tips; this quotient is expected to be very robust since it removes the inter-mitochondria variability. Fig. 3D shows that the quotient was > 1 for anterograde mitochondria whereas it was not significantly different from 1 for retrograde organelles in line with the results showed in Fig. 3C.

3.3 Numerical simulations predict slower exchange of motors at the leading tip during anterograde runs

To explore the predictions of a simple model that includes an elongated cargo transported by molecular motors that also diffuse on the organelle membrane (processes i and iv in Fig. 2C), we performed numerical simulations of kinesin motors attached to a one-dimensional, elongated cargo in the presence of increasing loads.

In these simulations, motors undergo one-dimensional diffusion on the cargo, attach to a linear track, step on it and detach with different probabilities. In line with previous observations [89] we considered that the detachment probability increases with both, resisting and assisting loads. Additionally, we assumed that each motor reaching a tip of the cargo is replaced by a new motor molecule in the opposite tip. Organelles in living cells are decorated with several motor molecules diffusing on its membrane. Thus, this periodic boundary condition resembles the natural injection of motors through diffusion at both organelle extremes.

We generated intensity kymographs from the simulated motor trajectories using the software FERNET [93] set in the line-scanning mode with parameters similar to those used in the experiments. These data were analyzed similarly to the experimental kymographs (Fig. 4A). In agreement with the experimental results, the simulated autocorrelation curves could be fitted

with an exponential decay function (Fig. 4B) also allowing the calculation of a characteristic residence time ($\tau_{r,sim}$).

Fig. 4C shows simulated cargoes trajectories and the mean autocorrelation curves obtained at the leading and rear positions of the cargo. The quantitative analysis of these data indicates that both $\tau_{r\ leading,sim}$ and $\tau_{r\ rear,sim}$ decrease with the load with an initial steeper slope in the leading tip (Fig. 4D). Simulations of a tug of war scenario leading to retrograde transport, also predict similar $\tau_{r,sim}$ values at the leading and rear regions (Supplemental Fig. 8).

We also ran simulations similar to those described in Fig. 4 but considering reflecting boundaries (i.e. motors that reach the farthest positions of the cargo bounce back). Despite these conditions generate some artifacts in the ACF analyses (Supplemental Fig. 9A-B), these simulations lead to results similar to those observed in Fig. 4 (Supplemental Fig. 9C-D).

To summarize, the numerical simulations agree with the experimental data and show that the exchange of motors at the leading and rear regions of the cargo depends on the transport direction.

4. Discussion

The *in vitro* behavior of molecular motors does not explain many properties of intracellular transport emphasizing the relevance of studying how these biomolecules work in their natural environment. Particularly, many evidences indicate that motors require working together to drag large cargoes in living cells and thus the transport performance depends on the motors disposition on the cargo and their communication, probably mediated by adaptor proteins and the organelle membrane [21, 23, 28].

Here, using a combination of single particle tracking and fluorescence fluctuations techniques we explored how motors organize on mitochondria while they move along microtubule bundles in cell processes in *Drosophila* S2 cells. These bundles provide almost rectilinear tracks for the transport and can be observed through line-scanning approaches which are faster than standard confocal imaging. In addition, the rod-like structure of mitochondria at processes simplifies both, tracking the organelles and studying the dynamics of the motors at different organelle regions.

For this study, we engineered an EGFP-tagged kinesin-1 heavy chain that includes the motor domains and that binds to adaptor proteins on cargoes directly or through a light chain [129]. The fusion protein interacted with both, microtubules and mitochondria and did not affect relevant properties of mitochondria transport. Winding et al. [130] performed KHC knockdown experiments followed by transient expression of KHC fused to a blue variant of GFP and showed

that the expression of this protein results in the recovery of both, the motor-dependent transport performance and the morphology of the microtubule network.

Two-color line scanning experiments along cell processes provide the position of MTDR-stained mitochondria with nanometer precision and simultaneously inform on KHC-EGFP intensity with millisecond resolution at different organelle positions. The temporal autocorrelation analysis of these intensity traces allows recovering quantitative information on how motors dynamically organize on the organelles while they actively move along microtubules.

This approach showed that the exchange of kinesin motors at the mitochondria surface during transport occurs in a temporal window of ~100 ms. Since directional runs last longer (~ 3 s, Supplemental Table 2), the processive motion of mitochondria probably requires the continuous replacement of those active motors that detach from the track and diffuse away on the organelle membrane. In line with this proposition, Leduc et al. [131] and Campas et al. [132] postulated a treadmilling mechanism to explain how kinesins anchored to the lipid bilayer work together during nanotubes extraction from giant unilamellar vesicles. According to this model, bulk motors diffusing in the nanotube replace those leading motors that stochastically detach from the microtubule track.

Our data also revealed that the relative dynamics of kinesin motors at the leading and rear regions of the mitochondria is different for anterograde and retrograde organelles. Specifically, retrograde organelles showed similar motor exchange rates in these regions whereas kinesin motors located at the tip of anterograde organelles remained anchored for longer periods of time in comparison to trailing motors. These results agree with *in vitro* observations showing that trailing myosin motors detach faster from the actin track when carrying synthetic lipid vesicles [23]. Based on numerical simulations, Nelson et al. [23] proposed that trailing motors experience assistive loads triggering their fast detachment from the track. In spite of the different characteristics of kinesin and myosin motors, assisting loads also increase the detachment probability of kinesin-1 [89] and could also explain the comparatively faster detachment of trailing motors verified during anterograde mitochondria transport. In addition, numerical simulations also predict that leading kinesins remain anchored to the track for longer periods of time than rear motors [133].

In line with this hypothesis, our numerical simulations of elongated-cargoes transport predict that leading motors spend longer periods of time bound to the track in comparison to rear motors during anterograde motion. Besides, these simulations also showed similar dwell times for kinesin motors at the leading and rear tips of the cargo during retrograde motion either caused by a high and constant load or by a winning opposed-polarity team. We must remind that in these simulations we considered a constant mechanical communication between motors only due to an elastic motor-organelle linker and a non-deformable cargo.

Our results could also be explained if the diffusion of motors on the organelle membrane is different at the leading and rear extremes of anterograde organelles and depends on the organelle speed. However, as far as we know, there are no experimental data evidencing heterogeneities at the level of organelle´s membrane that could support this model.

In recent years, it has been demonstrated that microtubules present several post-translational modifications (PTMs) that depend on the cell type, impact on several cellular functions [134-136] and are implicated in many diseases [137, 138]. PTMs and the different isoforms of tubulins are considered as a "tubulin-code" that generates microtubules with different properties allowing them to adapt to specific functions in essential cell processes [139-141].

The tubulin code is changing our view of intracellular transport. Initially considered as inert tracks, microtubules are now recognized as key elements for defining and controlling the asymmetrical distribution of organelles and other cargoes. Several PTMs affect the velocity and processivity of motors along microtubules [142]; relevantly, the modulation depended on the motor type. Particularly, the motility of kinesin-1 is affected by tubulin PTMs both *in vitro* and in cells [20, 143-146]. For example, Cai et al. [20] showed that this motor preferentially moves along acetylated and detyrosinated microtubules in cells whereas KIF17 and KIF1A are not as selective in their tracks. In neurons, the modulation of kinesins motility by different PTMs is central for the polarized sorting of cargoes [146, 147]. As far as we know, PTMs have not been explored in *Drosophila* S2 cells neither their relation to transport. In future works, it will be very interesting to address how different PTMs affect organelle transport in this cell line and asses if these modifications modulate the dynamics of teams of kinesins carrying together a cargo.

In conclusion, our work provides a detailed dynamical view of how kinesin motors organize during active transport of a cargo. This study also opens new questions on collective transport in living cells. Particularly, it would be relevant to explore (using, for example, the methodology designed in our work) how the fluidity of the organelle membrane, the cargo stiffness and its size affect the mechanical communication and therefore the dwell time of motors on the cytoskeletal track. This information could shed light on how motors and cytoskeleton work together during the translational and/or rotational motion of large intracellular cargoes.

Acknowledgements

This work was supported by ANPCyT [grant number PICT 2015-0370]; UBACyT [grant number 20020150100122BA]; and CONICET [grant number PIP 11220130100121CO].

References

[1] W.O. Hancock, Bidirectional cargo transport: moving beyond tug of war, Nat Rev Mol Cell Biol, 15 (2014) 615-628.

[2] M.A. Welte, Bidirectional transport along microtubules, Curr Biol, 14 (2004) R525-537.

[3] N. Hirokawa, Y. Noda, Y. Tanaka, S. Niwa, Kinesin superfamily motor proteins and intracellular transport, Nat Rev Mol Cell Biol, 10 (2009) 682-696.

[4] R.D. Vale, The molecular motor toolbox for intracellular transport, Cell, 112 (2003) 467-480.

[5] S.T. Brady, G.A. Morfini, Regulation of motor proteins, axonal transport deficits and adult-onset neurodegenerative diseases, Neurobiology of disease, 105 (2017) 273-282.

[6] S. Millecamps, J.P. Julien, Axonal transport deficits and neurodegenerative diseases, Nature reviews. Neuroscience, 14 (2013) 161-176.

[7] S. Maday, A.E. Twelvetrees, A.J. Moughamian, E.L. Holzbaur, Axonal transport: cargo-specific mechanisms of motility and regulation, Neuron, 84 (2014) 292-309.

[8] V. Belyy, M.A. Schlager, H. Foster, A.E. Reimer, A.P. Carter, A. Yildiz, The mammalian dynein-dynactin complex is a strong opponent to kinesin in a tug-of-war competition, Nat Cell Biol, 18 (2016) 1018-1024.

[9] A. Yildiz, M. Tomishige, R.D. Vale, P.R. Selvin, Kinesin walks hand-over-hand, Science, 303 (2004) 676-678.

[10] R. Mallik, B.C. Carter, S.A. Lex, S.J. King, S.P. Gross, Cytoplasmic dynein functions as a gear in response to load, Nature, 427 (2004) 649-652.

[11] S.L. Reck-Peterson, A. Yildiz, A.P. Carter, A. Gennerich, N. Zhang, R.D. Vale, Single-molecule analysis of dynein processivity and stepping behavior, Cell, 126 (2006) 335-348.

[12] K. Furuta, A. Furuta, Y.Y. Toyoshima, M. Amino, K. Oiwa, H. Kojima, Measuring collective transport by defined numbers of processive and nonprocessive kinesin motors, Proc Natl Acad Sci U S A, 110 (2013) 501-506.

[13] G. Arpag, S. Shastry, W.O. Hancock, E. Tuzel, Transport by populations of fast and slow kinesins uncovers novel family-dependent motor characteristics important for in vivo function, Biophys J, 107 (2014) 1896-1904.

[14] S.R. Norris, V. Soppina, A.S. Dizaji, K.I. Schimert, D. Sept, D. Cai, S. Sivaramakrishnan, K.J. Verhey, A method for multiprotein assembly in cells reveals independent action of kinesins in complex, J Cell Biol, 207 (2014) 393-406.

[15] K. Rezaul, D. Gupta, I. Semenova, K. Ikeda, P. Kraikivski, J. Yu, A. Cowan, I. Zaliapin, V. Rodionov, Engineered Tug-of-War Between Kinesin and Dynein Controls Direction of Microtubule Based Transport In Vivo, Traffic, 17 (2016) 475-486.

[16] Q. Li, K.F. Tseng, S.J. King, W. Qiu, J. Xu, A fluid membrane enhances the velocity of cargo transport by small teams of kinesin-1, J Chem Phys, 148 (2018) 123318.

[17] P. Sanghavi, A. D'Souza, A. Rai, A. Rai, R. Padinhatheeri, R. Mallik, Coin Tossing Explains the Activity of Opposing Microtubule Motors on Phagosomes, Curr Biol, 28 (2018) 1460-1466 e1464.

[18] S. Courty, C. Luccardini, Y. Bellaiche, G. Cappello, M. Dahan, Tracking individual kinesin motors in living cells using single quantum-dot imaging, Nano Lett, 6 (2006) 1491-1495.

[19] D. Cai, K.J. Verhey, E. Meyhofer, Tracking single Kinesin molecules in the cytoplasm of mammalian cells, Biophys J, 92 (2007) 4137-4144.

[20] D. Cai, D.P. McEwen, J.R. Martens, E. Meyhofer, K.J. Verhey, Single molecule imaging reveals differences in microtubule track selection between Kinesin motors, PLoS Biol, 7 (2009) e1000216.

[21] A. Rai, D. Pathak, S. Thakur, S. Singh, A.K. Dubey, R. Mallik, Dynein clusters into lipid microdomains on phagosomes to drive rapid transport toward lysosomes, Cell, 164 (2016) 722-734.

[22] R. Grover, J. Fischer, F.W. Schwarz, W.J. Walter, P. Schwille, S. Diez, Transport efficiency of membrane-anchored kinesin-1 motors depends on motor density and diffusivity, Proc Natl Acad Sci U S A, 113 (2016) E7185-E7193.

[23] S.R. Nelson, K.M. Trybus, D.M. Warshaw, Motor coupling through lipid membranes enhances transport velocities for ensembles of myosin Va, Proc Natl Acad Sci U S A, 111 (2014) E3986-3995.

[24] L. Kaplan, A. Ierokomos, P. Chowdary, Z. Bryant, B. Cui, Rotation of endosomes demonstrates coordination of molecular motors during axonal transport, Science advances, 4 (2018) e1602170.

[25] W. Lu, U. Del Castillo, V.I. Gelfand, Organelle transport in cultured Drosophila cells: S2 cell line and primary neurons, J Vis Exp, (2013) e50838.

[26] D.W. Buster, J. Nye, J.E. Klebba, G.C. Rogers, Preparation of Drosophila S2 cells for light microscopy, J Vis Exp, (2010).

[27] S. Ally, A.G. Larson, K. Barlan, S.E. Rice, V.I. Gelfand, Opposite-polarity motors activate one another to trigger cargo transport in live cells, J Cell Biol, 187 (2009) 1071-1082.

[28] M.C. De Rossi, D.E. Wetzler, L. Bensenor, M.E. De Rossi, M. Sued, D. Rodriguez, V. Gelfand, L. Bruno, V. Levi, Mechanical coupling of microtubule-dependent motor teams during peroxisome transport in Drosophila S2 cells, Biochim Biophys Acta, 1861 (2017) 3178-3189.

[29] S.C. Ling, P.S. Fahrner, W.T. Greenough, V.I. Gelfand, Transport of Drosophila fragile X mental retardation protein-containing ribonucleoprotein granules by kinesin-1 and cytoplasmic dynein, Proc Natl Acad Sci U S A, 101 (2004) 17428-17433.

[30] C. Kural, H. Kim, S. Syed, G. Goshima, V.I. Gelfand, P.R. Selvin, Kinesin and Dynein Move a Peroxisome in Vivo: A Tug-of-War or Coordinated Movement?, Science, 308 (2005) 1469-1472.

[31] H. Kim, S.C. Ling, G.C. Rogers, C. Kural, P.R. Selvin, S.L. Rogers, V.I. Gelfand, Microtubule binding by dynactin is required for microtubule organization but not cargo transport, J Cell Biol, 176 (2007) 641-651.

[32] L.B. Bensenor, K. Barlan, S.E. Rice, R.G. Fehon, V.I. Gelfand, Microtubule-mediated transport of the tumor-suppressor protein Merlin and its mutants, Proc Natl Acad Sci U S A, 107 (2010) 7311-7316.

[33] A.L. Jolly, H. Kim, D. Srinivasan, M. Lakonishok, A.G. Larson, V.I. Gelfand, Kinesin-1 heavy chain mediates microtubule sliding to drive changes in cell shape, Proc Natl Acad Sci U S A, 107 (2010) 12151-12156.

[34] K. Barlan, W. Lu, V.I. Gelfand, The microtubule-binding protein ensconsin is an essential cofactor of kinesin-1, Curr Biol, 23 (2013) 317-322.

[35] G.C. Rogers, N.M. Rusan, M. Peifer, S.L. Rogers, A multicomponent assembly pathway contributes to the formation of acentrosomal microtubule arrays in interphase Drosophila cells, Mol Biol Cell, 19 (2008) 3163-3178.

[36] B. Alberts, A. Johnson, J. Lewis, M. Raff, K. Roberts, P. Walter, The cytoskeleton, in: Molecular biology of the cell, Garland Science, 2002.

[37] J.R. McIntosh, Mitosis, Cold Spring Harbor perspectives in biology, 8 (2016).

[38] M. Kirschner, T. Mitchison, Beyond self-assembly: from microtubules to morphogenesis, Cell, 45 (1986) 329-342.

[39] E.H. Hinchcliffe, F.J. Miller, M. Cham, A. Khodjakov, G. Sluder, Requirement of a centrosomal activity for cell cycle progression through G1 into S phase, Science, 291 (2001) 1547-1550.

[40] A. Khodjakov, R.W. Cole, B.R. Oakley, C.L. Rieder, Centrosome-independent mitotic spindle formation in vertebrates, Curr Biol, 10 (2000) 59-67.

[41] R. Basto, J. Lau, T. Vinogradova, A. Gardiol, C.G. Woods, A. Khodjakov, J.W. Raff, Flies without centrioles, Cell, 125 (2006) 1375-1386.

[42] N.M. Mahoney, G. Goshima, A.D. Douglass, R.D. Vale, Making microtubules and mitotic spindles in cells without functional centrosomes, Curr Biol, 16 (2006) 564-569.

[43] M. Bettencourt-Dias, G. Goshima, RNAi in Drosophila S2 cells as a tool for studying cell cycle progression, Methods Mol Biol, 545 (2009) 39-62.

[44] G. Goshima, R.D. Vale, The roles of microtubule-based motor proteins in mitosis: comprehensive RNAi analysis in the Drosophila S2 cell line, J Cell Biol, 162 (2003) 1003-1016.

[45] G. Goshima, R. Wollman, S.S. Goodwin, N. Zhang, J.M. Scholey, R.D. Vale, N. Stuurman, Genes required for mitotic spindle assembly in Drosophila S2 cells, Science, 316 (2007) 417-421.

[46] R.D. Vale, J.A. Spudich, E.R. Griffis, Dynamics of myosin, microtubules, and Kinesin-6 at the cortex during cytokinesis in Drosophila S2 cells, J Cell Biol, 186 (2009) 727-738.

[47] S. Moutinho-Pereira, N. Stuurman, O. Afonso, M. Hornsveld, P. Aguiar, G. Goshima, R.D. Vale, H. Maiato, Genes involved in centrosome-independent mitotic spindle assembly in Drosophila S2 cells, Proc Natl Acad Sci U S A, 110 (2013) 19808-19813.

[48] N. Lecland, A. Debec, A. Delmas, S. Moutinho-Pereira, N. Malmanche, A. Bouissou, C. Dupre, A. Jourdan, B. Raynaud-Messina, H. Maiato, A. Guichet, Establishment and mitotic characterization of new Drosophila acentriolar cell lines from DSas-4 mutant, Biology open, 2 (2013) 314-323.

[49] S. Moutinho-Pereira, A. Debec, H. Maiato, Microtubule cytoskeleton remodeling by acentriolar microtubule-organizing centers at the entry and exit from mitosis in Drosophila somatic cells, Mol Biol Cell, 20 (2009) 2796-2808.

[50] S. Moutinho-Pereira, I. Matos, H. Maiato, Drosophila S2 cells as a model system to investigate mitotic spindle dynamics, architecture, and function, Methods Cell Biol, 97 (2010) 243-257.

[51] G. Goshima, Assessment of mitotic spindle phenotypes in Drosophila S2 cells, Methods Cell Biol, 97 (2010) 259-275.

[52] S. Mische, Y. He, L. Ma, M. Li, M. Serr, T.S. Hays, Dynein light intermediate chain: an essential subunit that contributes to spindle checkpoint inactivation, Mol Biol Cell, 19 (2008) 4918-4929.

[53] B. Orr, H. Bousbaa, C.E. Sunkel, Mad2-independent spindle assembly checkpoint activation and controlled metaphase-anaphase transition in Drosophila S2 cells, Mol Biol Cell, 18 (2007) 850-863.

[54] G. Goshima, R. Wollman, N. Stuurman, J.M. Scholey, R.D. Vale, Length control of the metaphase spindle, Curr Biol, 15 (2005) 1979-1988.

[55] G. Goshima, F. Nedelec, R.D. Vale, Mechanisms for focusing mitotic spindle poles by minus end-directed motor proteins, J Cell Biol, 171 (2005) 229-240.

[56] G. Goshima, R.D. Vale, Cell cycle-dependent dynamics and regulation of mitotic kinesins in Drosophila S2 cells, Mol Biol Cell, 16 (2005) 3896-3907.

[57] S.L. Rogers, G.C. Rogers, D.J. Sharp, R.D. Vale, Drosophila EB1 is important for proper assembly, dynamics, and positioning of the mitotic spindle, J Cell Biol, 158 (2002) 873-884.

[58] W. Li, T. Miki, T. Watanabe, M. Kakeno, I. Sugiyama, K. Kaibuchi, G. Goshima, EB1 promotes microtubule dynamics by recruiting Sentin in Drosophila cells, J Cell Biol, 193 (2011) 973-983.

[59] C.A. Johnston, K. Hirono, K.E. Prehoda, C.Q. Doe, Identification of an Aurora-A/PinsLINKER/Dlg spindle orientation pathway using induced cell polarity in S2 cells, Cell, 138 (2009) 1150-1163.

[60] G.A. Pavlova, A.V. Razuvaeva, J.V. Popova, E.N. Andreyeva, L.A. Yarinich, M.O. Lebedev, C. Pellacani, S. Bonaccorsi, M.P. Somma, M. Gatti, A.V. Pindyurin, The role of Patronin in Drosophila mitosis, BMC molecular and cell biology, 20 (2019) 7.

[61] A. Strunov, L.V. Boldyreva, E.N. Andreyeva, G.A. Pavlova, J.V. Popova, A.V. Razuvaeva, A.F. Anders, F. Renda, A.V. Pindyurin, M. Gatti, E. Kiseleva, Ultrastructural analysis of mitotic Drosophila S2 cells identifies distinctive microtubule and intracellular membrane behaviors, BMC Biol, 16 (2018) 68.

[62] M. Bettencourt-Dias, R. Giet, R. Sinka, A. Mazumdar, W.G. Lock, F. Balloux, P.J. Zafiropoulos, S. Yamaguchi, S. Winter, R.W. Carthew, M. Cooper, D. Jones, L. Frenz, D.M. Glover, Genome-wide survey of protein kinases required for cell cycle progression, Nature, 432 (2004) 980-987.

[63] M. Björklund, M. Taipale, M. Varjosalo, J. Saharinen, J. Lahdenperä, J. Taipale, Identification of pathways regulating cell size and cell-cycle progression by RNAi, Nature, 439 (2006) 1009-1013.

[64] D.C. Chan, Mitochondria: dynamic organelles in disease, aging, and development, Cell, 125 (2006) 1241-1252.

[65] A.J. Roger, S.A. Munoz-Gomez, R. Kamikawa, The Origin and Diversification of Mitochondria, Curr Biol, 27 (2017) R1177-R1192.

[66] X. Liu, D. Weaver, O. Shirihai, G. Hajnoczky, Mitochondrial 'kiss-and-run': interplay between mitochondrial motility and fusion-fission dynamics, Embo J, 28 (2009) 3074-3089.

[67] L.C. Woods, G.W. Berbusse, K. Naylor, Microtubules Are Essential for Mitochondrial Dynamics-Fission, Fusion, and Motility-in Dictyostelium discoideum, Frontiers in cell and developmental biology, 4 (2016) 19.

[68] S. Hoppins, The regulation of mitochondrial dynamics, Curr Opin Cell Biol, 29 (2014) 46-52.

[69] M. Nangaku, R. Sato-Yoshitake, Y. Okada, Y. Noda, R. Takemura, H. Yamazaki, N. Hirokawa, KIF1B, a novel microtubule plus end-directed monomeric motor protein for transport of mitochondria, Cell, 79 (1994) 1209-1220.

[70] Y. Tanaka, Y. Kanai, Y. Okada, S. Nonaka, S. Takeda, A. Harada, N. Hirokawa, Targeted disruption of mouse conventional kinesin heavy chain, kif5B, results in abnormal perinuclear clustering of mitochondria, Cell, 93 (1998) 1147-1158.

[71] A. Varadi, L.I. Johnson-Cadwell, V. Cirulli, Y. Yoon, V.J. Allan, G.A. Rutter, Cytoplasmic dynein regulates the subcellular distribution of mitochondria by controlling the recruitment of the fission factor dynamin-related protein-1, J Cell Sci, 117 (2004) 4389-4400.

[72] R.L. Frederick, J.M. Shaw, Moving mitochondria: establishing distribution of an essential organelle, Traffic, 8 (2007) 1668-1675.

[73] D.R. LaJeunesse, S.M. Buckner, J. Lake, C. Na, A. Pirt, K. Fromson, Three new Drosophila markers of intracellular membranes, BioTechniques, 36 (2004) 784-788, 790.

[74] R. Rizzuto, M. Brini, P. Pizzo, M. Murgia, T. Pozzan, Chimeric green fluorescent protein as a tool for visualizing subcellular organelles in living cells, Curr Biol, 5 (1995) 635-642.

[75] V. Levi, A.S. Serpinskaya, E. Gratton, V. Gelfand, Organelle transport along microtubules in Xenopus melanophores: evidence for cooperation between multiple motors, Biophys J, 90 (2006) 318-327.

[76] R. Bhat, J.A. Weaver, C. Wagner, J.E. Bodwell, E. Bresnick, ATP depletion affects the phosphorylation state, ligand binding, and nuclear transport of the 4 S polycyclic aromatic hydrocarbon-binding protein in rat hepatoma cells, J Biol Chem, 271 (1996) 32551-32556.

[77] M. Nakazawa, H. Matsubara, Y. Matsushita, M. Watanabe, N. Vo, H. Yoshida, M. Yamaguchi, T. Kataoka, The Human Bcl-2 Family Member Bcl-rambo Localizes to Mitochondria and Induces Apoptosis and Morphological Aberrations in Drosophila, PLoS One, 11 (2016) e0157823.

[78] T. Zhang, L. Xue, L. Li, C. Tang, Z. Wan, R. Wang, J. Tan, Y. Tan, H. Han, R. Tian, T.R. Billiar, W.A. Tao, Z. Zhang, BNIP3 Protein Suppresses PINK1 Kinase Proteolytic Cleavage to Promote Mitophagy, J Biol Chem, 291 (2016) 21616-21629.

[79] E.L. Elson, Brief introduction to fluorescence correlation spectroscopy, Methods Enzymol, 518 (2013) 11-41.

[80] J.R. Lakowicz, Principles of Fluorescence Spectroscopy, 3rd ed., Springer, 2006.

[81] M. Stortz, J. Angiolini, E. Mocskos, A. Wolosiuk, A. Pecci, V. Levi, Mapping the dynamical organization of the cell nucleus through fluorescence correlation spectroscopy, Methods, 140-141 (2018) 10-20.

[82] M. Stortz, D.M. Presman, L. Bruno, P. Annibale, M.V. Dansey, G. Burton, E. Gratton, A. Pecci, V. Levi, Mapping the Dynamics of the Glucocorticoid Receptor within the Nuclear Landscape, Sci Rep, 7 (2017) 6219.

[83] T. Wohland, R. Rigler, H. Vogel, The standard deviation in fluorescence correlation spectroscopy, Biophys J, 80 (2001) 2987-2999.

[84] A. Michelman-Ribeiro, D. Mazza, T. Rosales, T.J. Stasevich, H. Boukari, V. Rishi, C. Vinson, J.R. Knutson, J.G. McNally, Direct measurement of association and dissociation rates of DNA binding in live cells by fluorescence correlation spectroscopy, Biophys J, 97 (2009) 337-346.

[85] A. Kunwar, A. Mogilner, Robust transport by multiple motors with nonlinear force-velocity relations and stochastic load sharing, Phys Biol, 7 (2010) 16012.

[86] S. Bouzat, V. Levi, L. Bruno, Transport properties of melanosomes along microtubules interpreted by a tug-of-war model with loose mechanical coupling, PLoS One, 7 (2012) e43599.

[87] M.C. De Rossi, M.E. De Rossi, M. Sued, D. Rodriguez, L. Bruno, V. Levi, Asymmetries in kinesin-2 and cytoplasmic dynein contributions to melanosome transport, FEBS Lett, 589 (2015) 2763-2768.

[88] A. Kunwar, M. Vershinin, J. Xu, S.P. Gross, Stepping, strain gating, and an unexpected force-velocity curve for multiple-motor-based transport, Curr Biol, 18 (2008) 1173-1183.

[89] J.O. Andreasson, B. Milic, G.Y. Chen, N.R. Guydosh, W.O. Hancock, S.M. Block, Examining kinesin processivity within a general gating framework, Elife, 4 (2015).

[90] D.M. Owen, D.J. Williamson, A. Magenau, K. Gaus, Sub-resolution lipid domains exist in the plasma membrane and regulate protein diffusion and distribution, Nat Commun, 3 (2012) 1256.

[91] K. Luby-Phelps, Cytoarchitecture and physical properties of cytoplasm: volume, viscosity, diffusion, intracellular surface area, International review of cytology, 192 (2000) 189-221.

[92] B.R. Daniels, C.M. Hale, S.B. Khatau, S. Kusuma, T.M. Dobrowsky, S. Gerecht, D. Wirtz, Differences in the microrheology of human embryonic stem cells and human induced pluripotent stem cells, Biophys J, 99 (2010) 3563-3570.

[93] J.F. Angiolini, N. Plachta, E. Mocskos, V. Levi, Exploring the Dynamics of Cell Processes through Simulations of Fluorescence Microscopy Experiments, Biophys J, 108 (2015) 2613-2618.

[94] L. Wasserman, All of statistics: A concise course in statistical inference, Springer-Verlag, New York, 2010.

[95] A.F. Zuur, E.N. Ieno, C.S. Elphick, A protocol for data exploration to avoid common statistical problems, Methods in ecology and evolution, 1 (2010) 3-14.

[96] D.L. Coy, W.O. Hancock, M. Wagenbach, J. Howard, Kinesin's tail domain is an inhibitory regulator of the motor domain, Nat Cell Biol, 1 (1999) 288-292.

[97] D.S. Friedman, R.D. Vale, Single-molecule analysis of kinesin motility reveals regulation by the cargo-binding tail domain, Nat Cell Biol, 1 (1999) 293-297.

[98] M.F. Stock, J. Guerrero, B. Cobb, C.T. Eggers, T.G. Huang, X. Li, D.D. Hackney, Formation of the compact confomer of kinesin requires a COOH-terminal heavy chain domain and inhibits microtubule-stimulated ATPase activity, J Biol Chem, 274 (1999) 14617-14623.

[99] H.Y. Kaan, D.D. Hackney, F. Kozielski, The structure of the kinesin-1 motor-tail complex reveals the mechanism of autoinhibition, Science, 333 (2011) 883-885.

[100] K.A. Dietrich, C.V. Sindelar, P.D. Brewer, K.H. Downing, C.R. Cremo, S.E. Rice, The kinesin-1 motor protein is regulated by a direct interaction of its head and tail, Proc Natl Acad Sci U S A, 105 (2008) 8938-8943.

[101] D.D. Hackney, N. Baek, A.C. Snyder, Half-site inhibition of dimeric kinesin head domains by monomeric tail domains, Biochemistry, 48 (2009) 3448-3456.

[102] D.D. Hackney, M.F. Stock, Kinesin's IAK tail domain inhibits initial microtubule-stimulated ADP release, Nat Cell Biol, 2 (2000) 257-260.

[103] K.J. Verhey, N. Kaul, V. Soppina, Kinesin assembly and movement in cells, Annu Rev Biophys, 40 (2011) 267-288.

[104] A.L. Brittle, H. Ohkura, Mini spindles, the XMAP215 homologue, suppresses pausing of interphase microtubules in Drosophila, EMBO J, 24 (2005) 1387-1396.

[105] K.J. De Vos, J. Sable, K.E. Miller, M.P. Sheetz, Expression of phosphatidylinositol (4,5) bisphosphate-specific pleckstrin homology domains alters direction but not the level of axonal transport of mitochondria, Mol Biol Cell, 14 (2003) 3636-3649.

[106] A.D. Pilling, D. Horiuchi, C.M. Lively, W.M. Saxton, Kinesin-1 and Dynein are the primary motors for fast transport of mitochondria in Drosophila motor axons, Mol Biol Cell, 17 (2006) 2057-2068.

[107] S.L. Rogers, I.S. Tint, P.C. Fanapour, V.I. Gelfand, Regulated bidirectional motility of melanophore pigment granules along microtubules in vitro, Proc Natl Acad Sci U S A, 94 (1997) 3720-3725.

[108] A.R. Chaudhary, F. Berger, C.L. Berger, A.G. Hendricks, Tau directs intracellular trafficking by regulating the forces exerted by kinesin and dynein teams, Traffic, 19 (2018) 111-121.

[109] A.G. Hendricks, E.L. Holzbaur, Y.E. Goldman, Force measurements on cargoes in living cells reveal collective dynamics of microtubule motors, Proc Natl Acad Sci U S A, 109 (2012) 18447-18452.

[110] P. Barak, A. Rai, P. Rai, R. Mallik, Quantitative optical trapping on single organelles in cell extract, Nat Methods, 10 (2013) 68-70.

[111] A.K. Rai, A. Rai, A.J. Ramaiya, R. Jha, R. Mallik, Molecular adaptations allow dynein to generate large collective forces inside cells, Cell, 152 (2013) 172-182.

[112] K. Norregaard, R. Metzler, C.M. Ritter, K. Berg-Sorensen, L.B. Oddershede, Manipulation and Motion of Organelles and Single Molecules in Living Cells, Chem Rev, 117 (2017) 4342-4375.

[113] P. Schwille, E. Haustein, Fluorescence correlation spectroscopy. An introduction to its concepts and applications, in: Biophysics Textbook Online, 2001, pp. 1-33.

[114] S.T. Brady, K.K. Pfister, G.S. Bloom, A monoclonal antibody against kinesin inhibits both anterograde and retrograde fast axonal transport in squid axoplasm, Proc Natl Acad Sci U S A, 87 (1990) 1061-1065.

[115] S. Bhuvanendran, K. Salka, K. Rainey, S.C. Sreetama, E. Williams, M. Leeker, V. Prasad, J. Boyd, G.H. Patterson, J.K. Jaiswal, A.M. Colberg-Poley, Superresolution imaging of human cytomegalovirus vMIA localization in sub-mitochondrial compartments, Viruses, 6 (2014) 1612-1636.

[116] J.R. Stiles, D. Van Helden, T.M. Bartol, Jr., E.E. Salpeter, M.M. Salpeter, Miniature endplate current rise times less than 100 microseconds from improved dual recordings can be modeled with passive acetylcholine diffusion from a synaptic vesicle, Proc Natl Acad Sci U S A, 93 (1996) 5747-5752.

[117] R.A. Kerr, T.M. Bartol, B. Kaminsky, M. Dittrich, J.C. Chang, S.B. Baden, T.J. Sejnowski, J.R. Stiles, Fast Monte Carlo Simulation Methods for Biological Reaction-Diffusion Systems in Solution and on Surfaces, SIAM J Sci Comput, 30 (2008) 3126.

[118] J.R. Stiles, T.M. Bartol, Monte Carlo methods for simulating realistic synaptic microphysiology using MCell, in: E. De Schutter (Ed.) Computational Neuroscience: Realistic modeling for experimentalists, CRC Press, Boca Raton, 2001, pp. 87-127.

[119] B. Alberts, A. Johnson, J. Lewis, M. Raff, K. Roberts, P. Walter, The mitochondrion, in: Molecular biology of the cell, Garland Science, 2002.

[120] T. Appelhans, K.B. Busch, Dynamic imaging of mitochondrial membrane proteins in specific sub-organelle membrane locations, Biophysical reviews, 9 (2017) 345-352.

[121] V.M. Sukhorukov, D. Dikov, K. Busch, V. Strecker, I. Wittig, J. Bereiter-Hahn, Determination of protein mobility in mitochondrial membranes of living cells, Biochim Biophys Acta, 1798 (2010) 2022-2032.

[122] J.L. Cyr, K.K. Pfister, G.S. Bloom, C.A. Slaughter, S.T. Brady, Molecular genetics of kinesin light chains: generation of isoforms by alternative splicing, Proc Natl Acad Sci U S A, 88 (1991) 10114-10118.

[123] C. Di Rienzo, V. Piazza, E. Gratton, F. Beltram, F. Cardarelli, Probing short-range protein Brownian motion in the cytoplasm of living cells, Nat Commun, 5 (2014) 5891.

[124] H.W. Wu, T. Kuhn, V.T. Moy, Mechanical properties of L929 cells measured by atomic force microscopy: effects of anticytoskeletal drugs and membrane crosslinking, Scanning, 20 (1998) 389-397.

[125] V. Soppina, A.K. Rai, A.J. Ramaiya, P. Barak, R. Mallik, Tug-of-war between dissimilar teams of microtubule motors regulates transport and fission of endosomes, Proc Natl Acad Sci U S A, 106 (2009) 19381-19386.

[126] R. Rigler, U. Mets, J. Widengren, P. Kask, Fluorescence correlation spectroscopy with high count rate and low background: analysis of translational diffusion, Eur Biophys J, 22 (1993) 169-175.

[127] A. Gennerich, D. Schild, Fluorescence correlation spectroscopy in small cytosolic compartments depends critically on the diffusion model used, Biophys J, 79 (2000) 3294-3306.

[128] S. Klumpp, R. Lipowsky, Cooperative cargo transport by several molecular motors, Proc Natl Acad Sci U S A, 102 (2005) 17284-17289.

[129] F. Sun, C. Zhu, R. Dixit, V. Cavalli, Sunday Driver/JIP3 binds kinesin heavy chain directly and enhances its motility, EMBO J, 30 (2011) 3416-3429.

[130] M. Winding, M.T. Kelliher, W. Lu, J. Wildonger, V.I. Gelfand, Role of kinesin-1-based microtubule sliding in Drosophila nervous system development, Proc Natl Acad Sci U S A, 113 (2016) E4985-4994.

[131] C. Leduc, O. Campas, K.B. Zeldovich, A. Roux, P. Jolimaitre, L. Bourel-Bonnet, B. Goud, J.F. Joanny, P. Bassereau, J. Prost, Cooperative extraction of membrane nanotubes by molecular motors, Proc Natl Acad Sci U S A, 101 (2004) 17096-17101.

[132] O. Campas, C. Leduc, P. Bassereau, J. Casademunt, J.F. Joanny, J. Prost, Coordination of Kinesin motors pulling on fluid membranes, Biophys J, 94 (2008) 5009-5017.

[133] W. Nam, B.I. Epureanu, Highly loaded behavior of kinesins increases the robustness of transport under high resisting loads, PLoS Comput Biol, 11 (2015) e1003981.

[134] A. Roll-Mecak, How cells exploit tubulin diversity to build functional cellular microtubule mosaics, Curr Opin Cell Biol, 56 (2019) 102-108.

[135] M.M. Magiera, P. Singh, C. Janke, SnapShot: Functions of Tubulin Posttranslational Modifications, Cell, 173 (2018) 1552-1552 e1551.

[136] C. Janke, J.C. Bulinski, Post-translational regulation of the microtubule cytoskeleton: mechanisms and functions, Nat Rev Mol Cell Biol, 12 (2011) 773-786.

[137] M.M. Magiera, P. Singh, S. Gadadhar, C. Janke, Tubulin Posttranslational Modifications and Emerging Links to Human Disease, Cell, 173 (2018) 1323-1327.

[138] C.P. Garnham, A. Roll-Mecak, The chemical complexity of cellular microtubules: tubulin post-translational modification enzymes and their roles in tuning microtubule functions, Cytoskeleton (Hoboken), 69 (2012) 442-463.

[139] S. Gadadhar, S. Bodakuntla, K. Natarajan, C. Janke, The tubulin code at a glance, J Cell Sci, 130 (2017) 1347-1353.

[140] C. Janke, The tubulin code: molecular components, readout mechanisms, and functions, J Cell Biol, 206 (2014) 461-472.

[141] K.J. Verhey, J. Gaertig, The tubulin code, Cell Cycle, 6 (2007) 2152-2160.

[142] M. Sirajuddin, L.M. Rice, R.D. Vale, Regulation of microtubule motors by tubulin isotypes and post-translational modifications, Nat Cell Biol, 16 (2014) 335-344.

[143] N. Kaul, V. Soppina, K.J. Verhey, Effects of alpha-tubulin K40 acetylation and detyrosination on kinesin-1 motility in a purified system, Biophys J, 106 (2014) 2636-2643.

[144] N.A. Reed, D. Cai, T.L. Blasius, G.T. Jih, E. Meyhofer, J. Gaertig, K.J. Verhey, Microtubule acetylation promotes kinesin-1 binding and transport, Curr Biol, 16 (2006) 2166-2172.

[145] D.V. Lessard, O.J. Zinder, T. Hotta, K.J. Verhey, R. Ohi, C.L. Berger, Polyglutamylation of tubulin's C-terminal tail controls pausing and motility of kinesin-3 family member KIF1A, J Biol Chem, 294 (2019) 6353-6363.

[146] J.W. Hammond, C.F. Huang, S. Kaech, C. Jacobson, G. Banker, K.J. Verhey, Posttranslational modifications of tubulin and the polarized transport of kinesin-1 in neurons, Mol Biol Cell, 21 (2010) 572-583.

[147] R.P. Tas, A. Chazeau, B.M.C. Cloin, M.L.A. Lambers, C.C. Hoogenraad, L.C. Kapitein, Differentiation between Oppositely Oriented Microtubules Controls Polarized Neuronal Transport, Neuron, 96 (2017) 1264-1271 e1265.

FIGURES CAPTIONS

Fig. 1. KHC-EGFP binds to mitochondria and microtubule tracks in *Drosophila* S2 cells. (**A**) Confocal images of a S2 cell transfected with the pMT-KHC-EGFP vector (green) and incubated with MTDR (red). The green image was obtained by averaging a 200-image stack collected at 0.3 frames/s whereas the red image corresponds to the first image of the stack (top panel). Zoom-in region of the same cell showing the enrichment of fluorescent motor molecules in microtubule-like filaments (bottom panel). Scale bar: 5 μm. (**B**) Snapshots of a movie illustrating the active motion of a mitochondrion (arrow) along a process. Scale bar: 3 μm. (**C**) Snapshots obtained from the time-lapse stack of a cell process (yellow rectangle in A) showing the green (top) and green-red merged (bottom) images. The right panels show the intensity profiles along the process; arrows indicate the positions of the organelles determined from the MTDR signal. Scale bar: 3 μm. (**D**) Confocal images of a mitochondria-enriched suspension. Colocalization of the KHC-EGFP and MTDR appears in yellow in the merge image. Scale bar: 3 μm.

Fig. 2. The combination of line-FCS and single particle tracking allow studying KHC-EGFP dynamics during mitochondria transport. (**A**) The confocal microscope was set to repetitively scan the laser in a linear pattern along a process presenting a mitochondrion (left panel). Example of the kymograph obtained for the red channel showing a processive retrograde run (dotted yellow box in the right panel). The mitochondrion position obtained line-by-line by a sub-pixel tracking routine was used to generate centered red (MTDR) and green (KHC-EGFP) kymographs as detailed in Supplementary Materials. Scale bar: 2 μm. (**B**) Representative intensity trace and the autocorrelation curve obtained at a position close to the leading end of a mitochondrion. The continuous line represents the fit of Eq. 4 with $\tau_r = 150 \pm 20$ ms. (**C**) Schematic representation of the dynamical processes involving EGFP-labeled motor molecules. Motors (blue) may diffuse on the organelle membrane (i), bind/unbind from the organelle (ii), diffuse in the intracellular milieu in a folded, autoinhibited conformation (iii) or carry an organelle along the track (iv). The red oval represents a mitochondrion actively transported along a microtubule; the small red dots on the organelle correspond to biomolecules mediating the binding of motors to the organelle. The green shape represents the laser beam of the confocal microscope. (**D**) Representative autocorrelation function curve (black line) obtained in a single point FCS experiment run in a S2 cell expressing KHC-EGFP. The gray and blue lines show the fast and slow components obtained from fitting the data with a two-component diffusion model (Eq.2). (**E**) Residence time of KHC-EGFP (τ_r) determined for slow and fast anterograde mitochondria. Data are presented as median ± S.E. (N_{slow}=51 and N_{fast}=102). Asterisk denotes significant differences between values (p-value<0.05).

Fig. 3. KHC-EGFP exhibits different dynamics at the leading and rear regions of mitochondria. (**A**) Overlay of centered green and red kymographs obtained after tracking a mitochondrion during an anterograde run. The autocorrelation of KHC-EGFP intensity was calculated pixel-by-pixel within a

region of the green kymograph and represented in pseudocolor. The black line on top of the matrix represents the intensity collected in the red channel along de organelle. Scale bars, 1 μm. (**B**) Representative examples of the autocorrelation functions calculated at the leading (blue) and rear (magenta) end of an organelle during the anterograde run. (**C**) Characteristic dwell time at the leading (blue) and rear (magenta) edge of mitochondria during anterograde (dark colors) and retrograde (light colors) runs. Data are presented as median ± S.E. (anterograde: $N_{leading}$ = 68 and N_{rear} = 62, retrograde: $N_{leading}$ = 64 and N_{rear} = 73). Asterisk denotes significant differences between values (p-value<0.05). (**D**) Quotient between τ_r values measured in single mitochondria at the leading and rear tips during anterograde (a) and retrograde (r) transport. The dotted line indicates a ratio equal to 1. ‡ indicates that $\tau_{leading}$ /τ_{rear} is significantly higher than 1. Data are presented as mean ± S.E ($N_{anterograde}$ = 41 and $N_{retrograde}$ = 43). Statistical analysis was performed using the one-sample t-test (p-value < 0.05).

Fig. 4. Numerical simulations reveal a different motor exchange at the mitochondria opposed edges during transport. (**A**) Output of numerical simulations showing the positions of the simulated motors (colored lines) and the cargo (black line) as a function of time. The dotted gray lines represent the cargo extremes. These data were re-centered at the cargo mean position and used as input in the software FERNET to generate a green kymograph. (**B**) The data were analyzed to obtain autocorrelation functions curves at cargo positions; the continuous black line indicates the fit of Eq 4 (top panel). Residuals obtained from the fitting are also shown (bottom panel). (**C**) Normalized autocorrelation functions (top panels) and trajectories (bottom panels) of the cargo recovered at leading (blue) and rear (magenta) regions at different loads. (**D**) Characteristic residence times at the leading (blue) and rear (magenta) extremes as a function of the load. The farthest pixels were not included in the analyses due to the slight deviations of the ACF data at these positions described in Supplemental Fig. 9. Data are presented as median ± S.E.

Credit Author Statement

De Rossi, MC et al

María Cecilia De Rossi: Conceptualization, Formal Analysis, Investigation, Writing – Original Draft, Writing – Review & Editing, Visualization. **Nicolás González Bardeci:** Formal Analysis, Investigation, Writing – Review & Editing. **Yanina Álvarez:** Formal Analysis, Writing – Review & Editing. **Esteban Mocksos:** Software, Visualization. **Juan José Romero:** Investigation. **Luciana Bruno:** Conceptualization, Methodology, Software, Formal Analysis, Writing – Original Draft, Writing – Review & Editing. **Diana Elena Wetzler:** Conceptualization, Methodology, Formal Analysis, Investigation, Writing – Original Draft, Writing – Review & Editing. **Valeria Levi:** Conceptualization, Methodology, Formal Analysis, Writing – Original Draft, Writing – Review & Editing, Visualization, Supervision, Project Administration.

Graphical abstract

Highlights

De Rossi, MC et al

Molecular motors actively transport organelles through the crowded cytoplasm

Kinesins dynamics at organelles was studied by fluorescence correlation spectroscopy

Our data reveals that motors exchange faster when organelles move at higher speeds

The exchange of leading and trailing motors depends on the transport direction

This study provides insights on the dynamical organization of motors on organelles

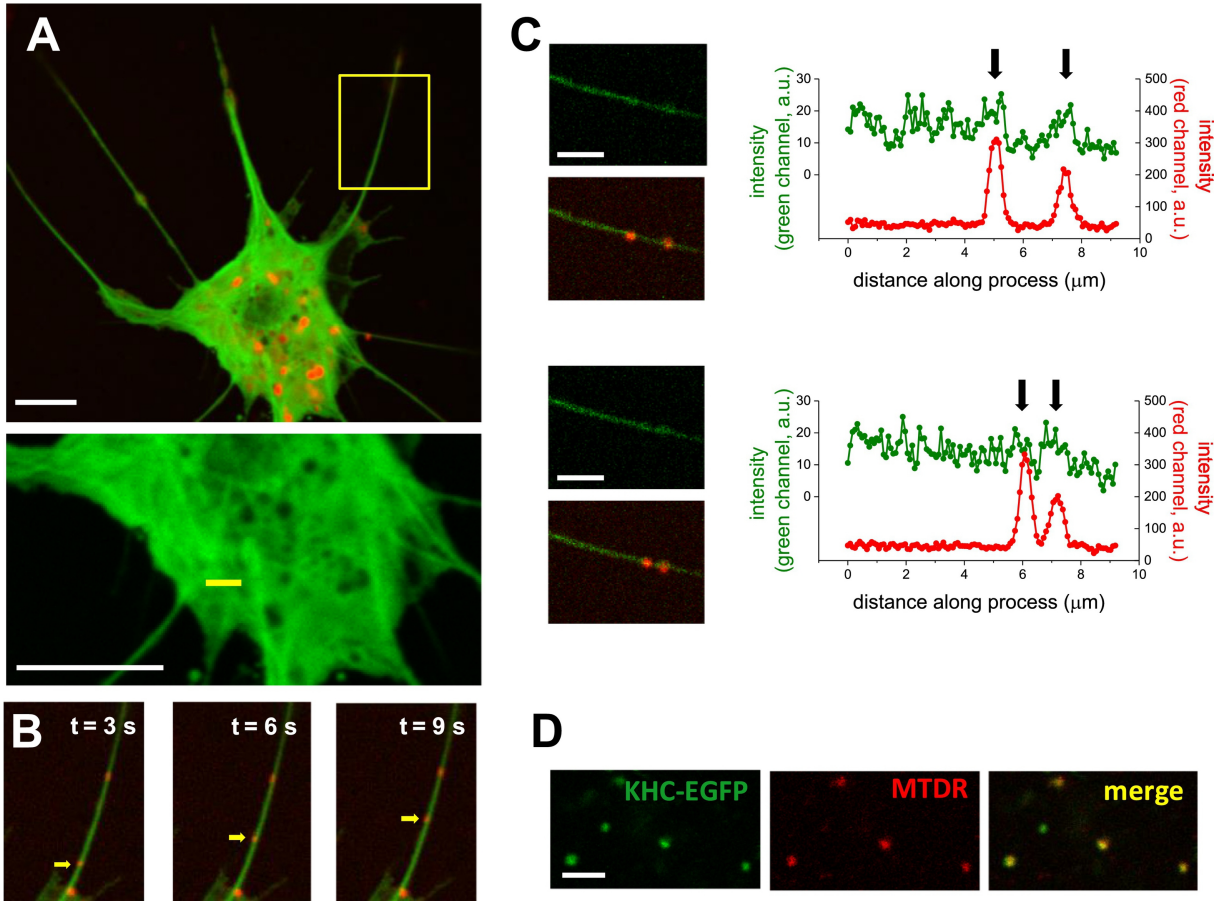
A
B
t = 3 s
t = 6 s
t = 9 s
C
intensity (green channel, a.u.)
intensity (red channel, a.u.)
distance along process (μm)
intensity (green channel, a.u.)
intensity (red channel, a.u.)
distance along process (μm)
D
KHC-EGFP
MTDR
merge

Figure 1

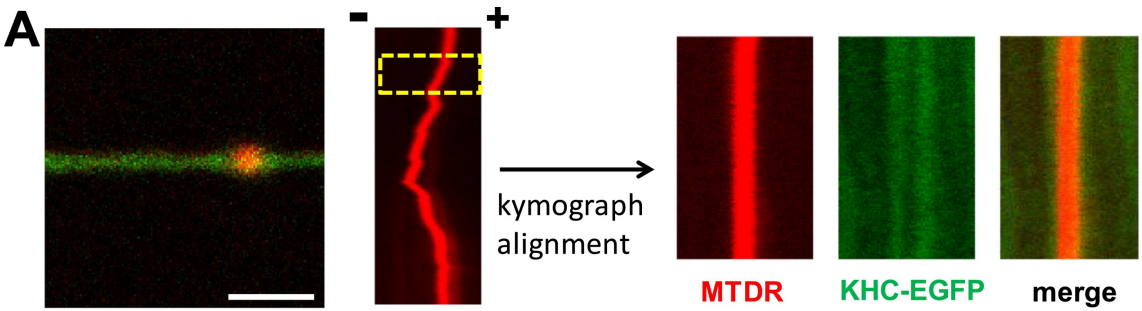
A
-
+
kymograph
alignment
MTDR
KHC-EGFP
merge

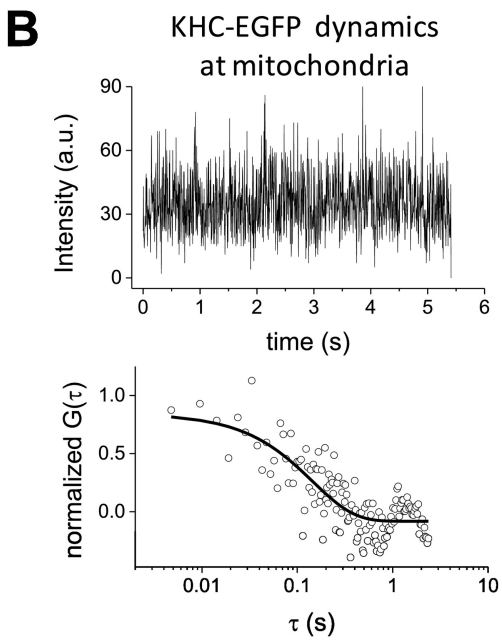
B
KHC-EGFP dynamics
at mitochondria
Intensity (a.u.)
time (s)
normalized G(τ)
τ (s)

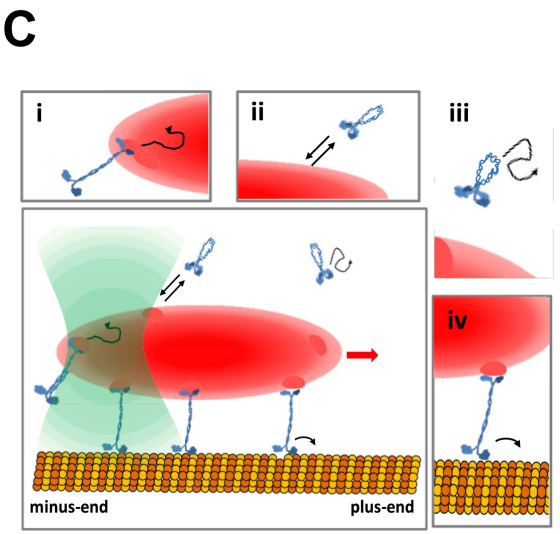
C
i
ii
iii
iv
minus-end
plus-end

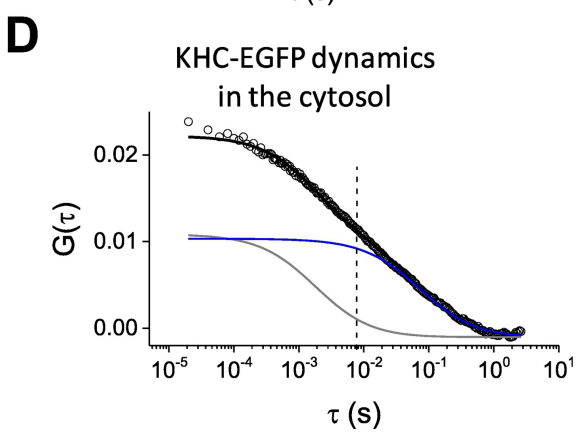
D
KHC-EGFP dynamics
in the cytosol
G(τ)
τ (s)

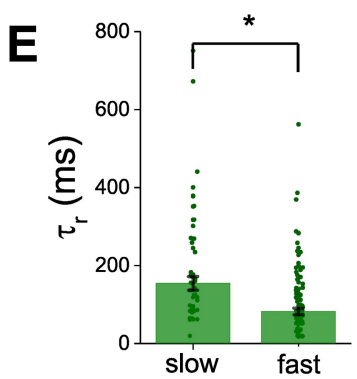
E
*
τr (ms)
slow
fast

Figure 2

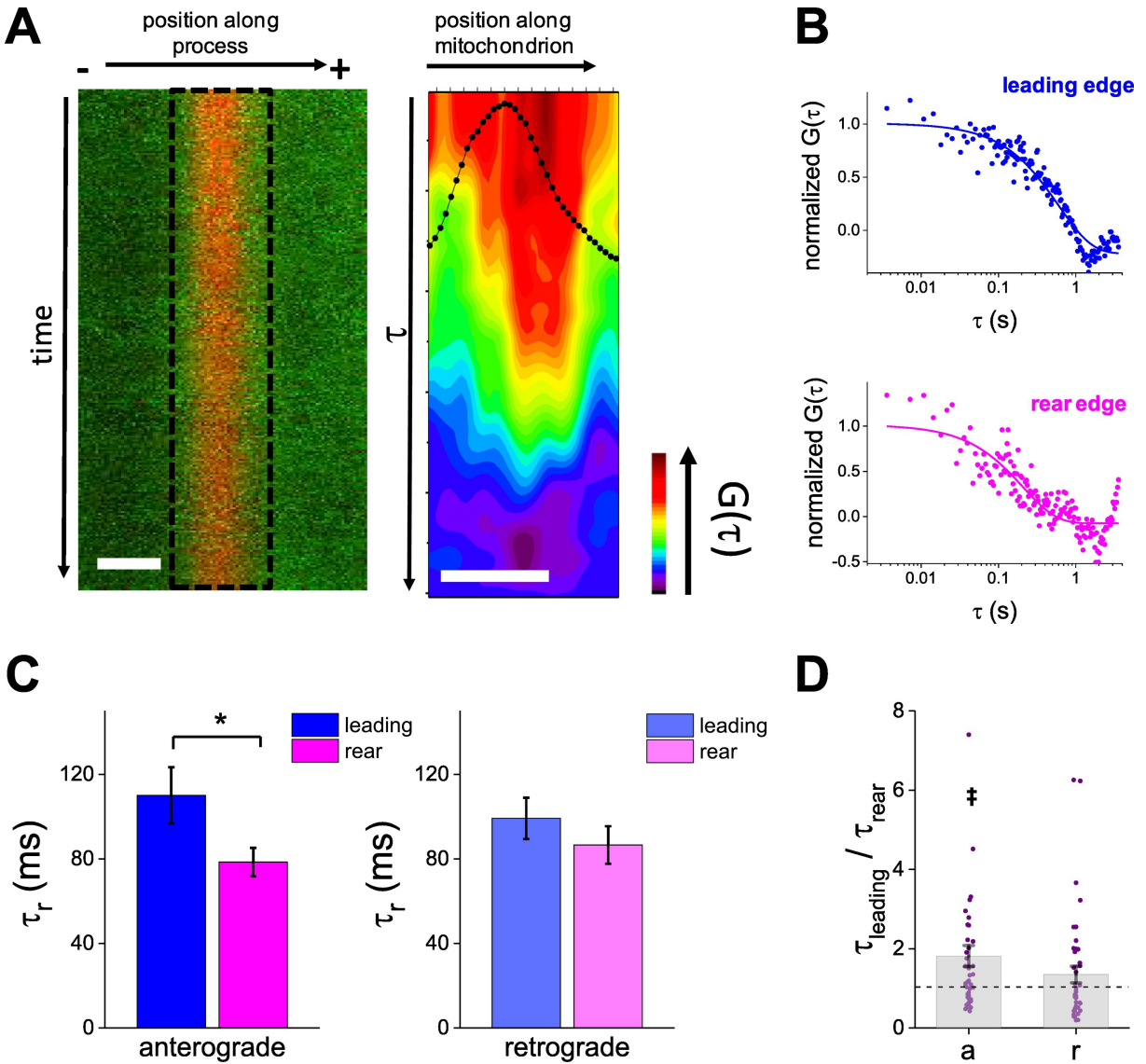
A
position along process
-
+
time
position along mitochondrion
τ
G(τ)
B
leading edge
normalized G(τ)
1.0
0.5
0.0
0.01
0.1
1
τ (s)
rear edge
normalized G(τ)
1.0
0.5
0.0
-0.5
0.01
0.1
1
τ (s)
C
*
leading
rear
τr (ms)
120
80
40
0
anterograde
leading
rear
τr (ms)
120
80
40
0
retrograde
D
τleading / τrear
8
6
4
2
0
‡
a
r

Figure 3

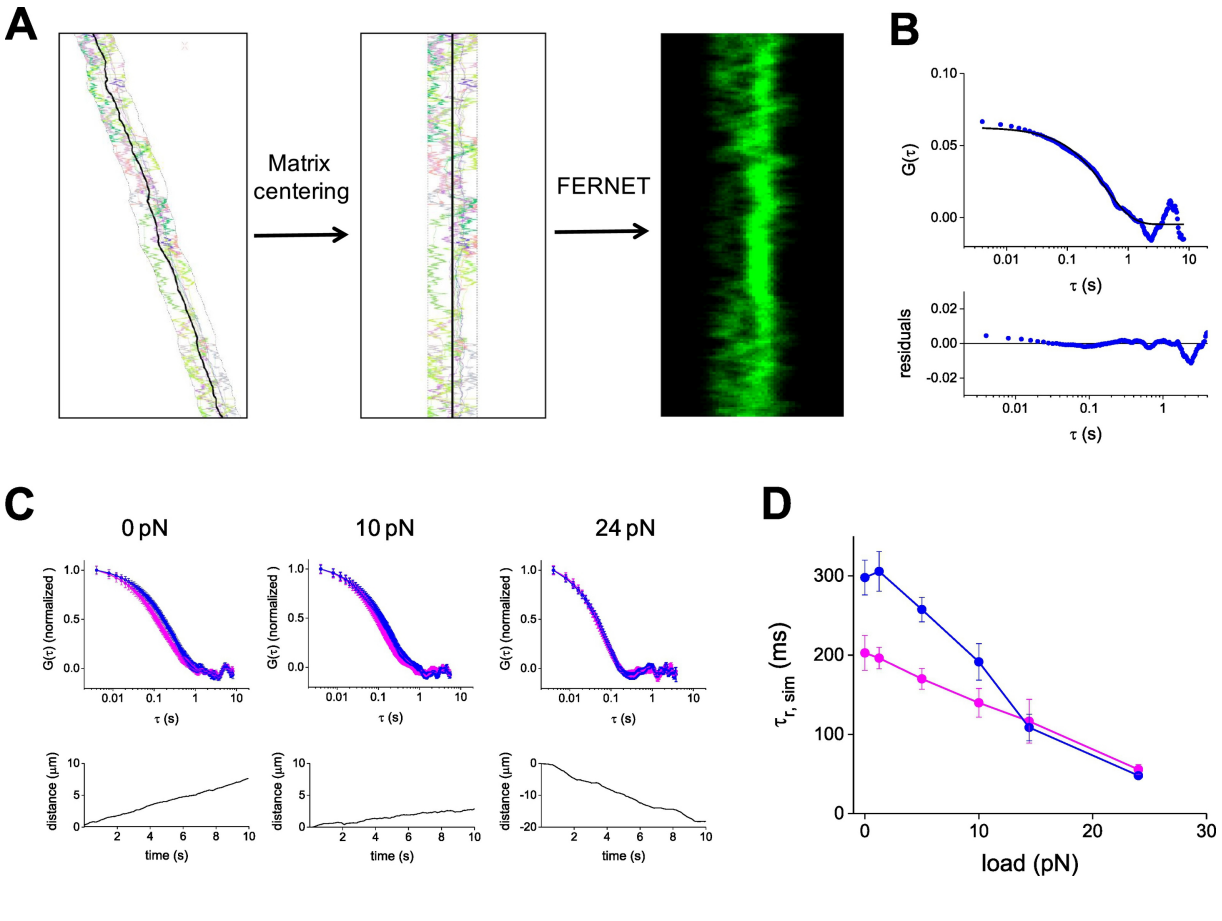
A
Matrix centering
FERNET
B
G(τ)
τ (s)
residuals
C
0 pN
10 pN
24 pN
G(τ) (normalized)
distance (μm)
time (s)
D
τr, sim (ms)
load (pN)

Figure 4